Evidence for surface water ice in the lunar polar regions using reflectance measurements from the Lunar Orbiter Laser Altimeter and temperature measurements from the Diviner Lunar Radiometer Experiment

Elizabeth A. Fisher[a,b], Paul G. Lucey[a,*], Myriam Lemelin[c], Benjamin T. Greenhagen[d], Matthew A. Siegler[e,f], Erwan Mazarico[g], Oded Aharonson[h], Jean-Pierre Williams[i], Paul O. Hayne[j], Gregory A. Neumann[g], David A. Paige[i], David E Smith[k], Maria T. Zuber[k]

[a] Hawaii Institute of Geophysics and Planetology, University of Hawaii at Manoa, 1680 East West Road, Honolulu HI 96822, USA
[b] Brown University, Department of Earth, Environmental & Planetary Sciences, 324 Brook St., Providence, RI 02912, USA
[c] Department of Earth & Space Science & Engineering, York University, Toronto, Canada
[d] Johns Hopkins University Applied Physics Laboratory, 11101 Johns Hopkins Rd., Laurel, 20723 MD, USA
[e] Planetary Science Institute, Tucson, Arizona 85719, USA
[f] Southern Methodist University, Dallas, Texas 75275, USA
[g] NASA Goddard Space Flight Center, Greenbelt, MD 20771
[h] Weizmann Institute of Science, Department of Earth and Planetary Sciences, Rehovot 76100, Israel
[i] Earth, Planetary, and Space Sciences, University of California, Los Angeles, CA 90095, United States
[j] Jet Propulsion Laboratory, California Institute of Technology, Pasadena, CA 91109, United States
[k] Department of Earth, Atmospheric and Planetary Sciences, MIT, 77 Massachusetts Ave., Cambridge, MA 02139, United States

ARTICLE INFO

ABSTRACT

We find that the reflectance of the lunar surface within 5° of latitude of the South Pole increases rapidly with decreasing temperature, near ~110 K, behavior consistent with the presence of surface water ice. The North polar region does not show this behavior, nor do South polar surfaces at latitudes more than 5° from the pole. This South pole reflectance anomaly persists when analysis is limited to surfaces with slopes less than 10° to eliminate false detection due to the brightening effect of mass wasting, and also when the very bright south polar crater Shackleton is excluded from the analysis. We also find that south polar regions of permanent shadow that have been reported to be generally brighter at 1064 nm do not show anomalous reflectance when their annual maximum surface temperatures are too high to preserve water ice. This distinction is not observed at the North Pole. The reflectance excursion on surfaces with maximum temperatures below 110 K is superimposed on a general trend of increasing reflectance with decreasing maximum temperature that is present throughout the polar regions in the north and south; we attribute this trend to a temperature or illumination-dependent space weathering effect (e.g. Hemingway et al., 2015). We also find a sudden increase in reflectance with decreasing temperature superimposed on the general trend at 200 K and possibly at 300 K. This may indicate the presence of other volatiles such as sulfur or organics. We identified and mapped surfaces with reflectances so high as to be unlikely to be part of an ice-free population. In this south we find a similar distribution found by Hayne et al. (2015) based on UV properties. In the north a cluster of pixels near that pole may represent a limited frost exposure.

1. Introduction

The possibility of water ice at the lunar poles was first proposed by Goddard (1920). Urey (1952) noted that the low lunar obliquity would give rise to surfaces permanently sheltered from sunlight, allowing the retention of volatiles and Watson et al. (1961) conducted the first scientific study of these regions on the Moon. Direct detection of anomalous volatile concentrations at the poles was reported by Feldman et al. (2001) on the basis of orbital neutron spectroscopy and later confirmed by Mitrofanov et al. (2012).

The planet Mercury also exhibits low obliquity. The Mercury Laser Altimeter (MLA) aboard the MESSENGER spacecraft revealed high reflectance material nearly exclusively occurring on permanently shadowed surfaces near Mercury's north pole where modeled biannual maximum surface temperatures do not exceed ∼100 K (Neumann et al., 2013; Paige et al., 2013). The use of maximum temperature by Neumann et al. (2013) and Paige et al. (2013) on Mercury polar data allowed reflectance anomalies to be interpreted in a physical-chemical context, which facilitated confident interpretation of Mercury's polar bright patches as being composed of water ice. Further evidence of bright surface ice has been found by long exposure imaging using the MESSENGER imaging system (Chabot et al., 2014), which also show a strong correlation of high surface reflectance with model maximum surface temperatures below ∼100 K.

The sublimation rate of water ice is exponentially dependent upon temperature and prevents surfaces that experience temperatures much above 100 K from preserving surface water ice due to rapid sublimation loss (e.g. Andreas, 2007). Conversely, surfaces that never exceed temperatures ∼100 K are able to preserve surface frost over geologically significant time periods against sublimation. For example, at 100 K, a 1 mm thick layer of water ice will persist for over 2 billion years against sublimation, whereas at 125 K the same layer will only persist about 1000 years. Even short periods of time at high temperatures would completely sublimate a surface deposit depending upon its thickness (Schorghofer and Taylor, 2007; Zhang and Paige, 2009; Paige et al., 2013), implying that the maximum temperature a surface experiences should predict the distribution and extent of volatile preservation on a planet's surface. This simple principle is complicated by volatile accumulation and loss rates, and by the thickness of initial deposits (e.g. Hayne et al., 2015), but Mercury shows that sublimation rate, controlled by temperature, can control the distribution of surface volatiles.

On the Moon, evidence for surface ice has been less clear, though Hayne et al. (2015) found that some areas in the lunar south pole with maximum surface temperatures below ∼100 K showed UV reflectance ratio values consistent with the presence of water ice using multispectral UV data from Lyman Alpha Mapping Project (LAMP) instrument aboard the Lunar Reconnaissance Orbiter (LRO) (Gladstone et al., 2010). Thin layers of surface ice would not be detectable by the lunar orbital neutron instruments. Scaling from the results of Lawrence et al. (2011), patchy ice layers less than about a millimeter thick would not produce a significant signal in current data, though detailed modeling of the neutron signature of thin surface layers of pure water ice has not been carried out.

Like MESSENGER, LRO carries a laser altimeter, the Lunar Orbiter Laser Altimeter (LOLA) (Smith et al., 2010), which also characterizes surface reflectance at 1064 nm (Zuber et al., 2012; Lucey et al., 2014; Lemelin et al., 2016). Combined with surface temperature data directly measured by the Diviner Lunar Radiometer (Paige et al., 2010a, 2010b), we can determine if the relationship between maximum temperature and reflectance indicates that surface water ice is present as it does on Mercury.

2. Data

The principal data sets used here are lunar surface reflectance at 1064 nm derived from LOLA, and maximum temperatures measured by Diviner. Images of the data used are shown the online supplemental material. The LOLA data used are that recently recalibrated by Lemelin et al. (2016) and are in units of normal albedo, which is the reflectance of the surface measured at zero phase angle relative to a Lambert surface illuminated at the same geometry. At zero phase, normal albedo and I/F

are equivalent. The data can be found on the LOLA PDS Data Node at: ⟨http://pds-geosciences.wustl.edu/lro/lro-l-lola-3-rdr-v1/lrolol_1xxx/data/⟩ in the directory labeled: "lola_radr", and detailed Information regarding the albedo data set and format descriptions in this archive can be found in the form of ASCII text files at: ⟨http://pds-geosciences.wustl.edu/lro/lro-l-lola-3-rdrv1/lrolol_1xxx/catalog/radr_ds.cat⟩ and ⟨http://pds-geosciences.wustl.edu/lro/lro-l-lola-3-rdr-v1/lrolol_1xxx/label/lolaradr.fmt⟩

Additional information regarding the processing and its usage can be found in Lemelin et al. (2016). Data within 5° of each pole were not directly calibrated by the methods of Lemelin et al. (2016), but rather are scaled to the global LOLA reflectance data set. The LOLA instrument experiences a strong anomaly related to the average surface temperature below the LRO spacecraft that is pertinent to the study reported here. As the spacecraft approaches the pole from the day side the lunar radiant emission drops, and insulating blankets surrounding the instrument contract due to the falling temperature. This contraction eventually pulls the LOLA transmit and receive telescopes out of alignment, causing the images of the five returning laser pulses to move off their five detectors resulting in a complete loss of signal. Fortuitously, as contraction continues, two of the five laser spots are directed onto two of the neighboring detectors, causing a return of signal. This divides LOLA data into a "day mode" (LRO over the illuminated moon) when returning laser shots arrive at their intended detectors, and a "night mode" (LRO on the night side of the Moon) when two of the returning laser shots are at least partially sampled by two neighboring detectors. There is the implicit third mode when no lunar ranging or reflectance data are returned at all; this occurs near the terminator at the poles, and all latitudes when the LRO orbit is near the beta = 90 condition (orbiting over the terminator). Because of this effect, on the majority of orbits useful reflectance data are not collected near the pole. However, during local winter, the illumination near the pole is limited and radiant heat load is low, so LOLA transitions into "night mode" while approaching the pole, and usable data are collected. Lemelin et al. (2016) used the substantial latitude overlap between the limited "night mode" polar data and the well-calibrated "day mode" data to transfer the calibration to the polar "night mode" data used here.

Temperature data are from the Diviner Lunar Radiometer (Diviner), a nine channel thermal infrared radiometer on LRO (Paige et al., 2010b). Seven of Diviner's channels measure emitted radiation between approximately 8 and 500 μm and these data can be combined to estimate the bolometric temperature of the surface (Paige et al., 2010a). LRO's polar orbit yields high resolution–roughly 250 m–temperature maps of the polar regions. More than seven years of Diviner operations combined with LRO's non-Sun-synchronous orbit allow for detailed maps to be produced as a function of time of day and season. We used bolometric temperature maps binned in 15 min local time increments (minutes scaled to the length of the lunar day) to produce a measurements of maximum and average surface temperature used in this study.

Supporting data sets used in this study are the surface slope and the average illumination of each location in the polar region to define the extent of permanently shadowed regions (PSRs). Surface slope values were computed from LOLA topographic data with the Generic Mapping Tools' `grdgradient` program (Wessel and Smith, 1991), and reflect the bi-directional slopes at a baseline of the resolution of the input elevation map (240 m). For illumination we turned to the numerical modeling tools developed by Mazarico et al. (2011). Following their methods, we first created horizon elevation maps from the LOLA polar topographic maps. We used more recent maps than in their original study, with a resolution of 240 m/pixel and covering each polar cap over latitudes 65°−90°, available at the NASA PDS Geosciences node. In addition to these average illumination maps, we computed the illumination
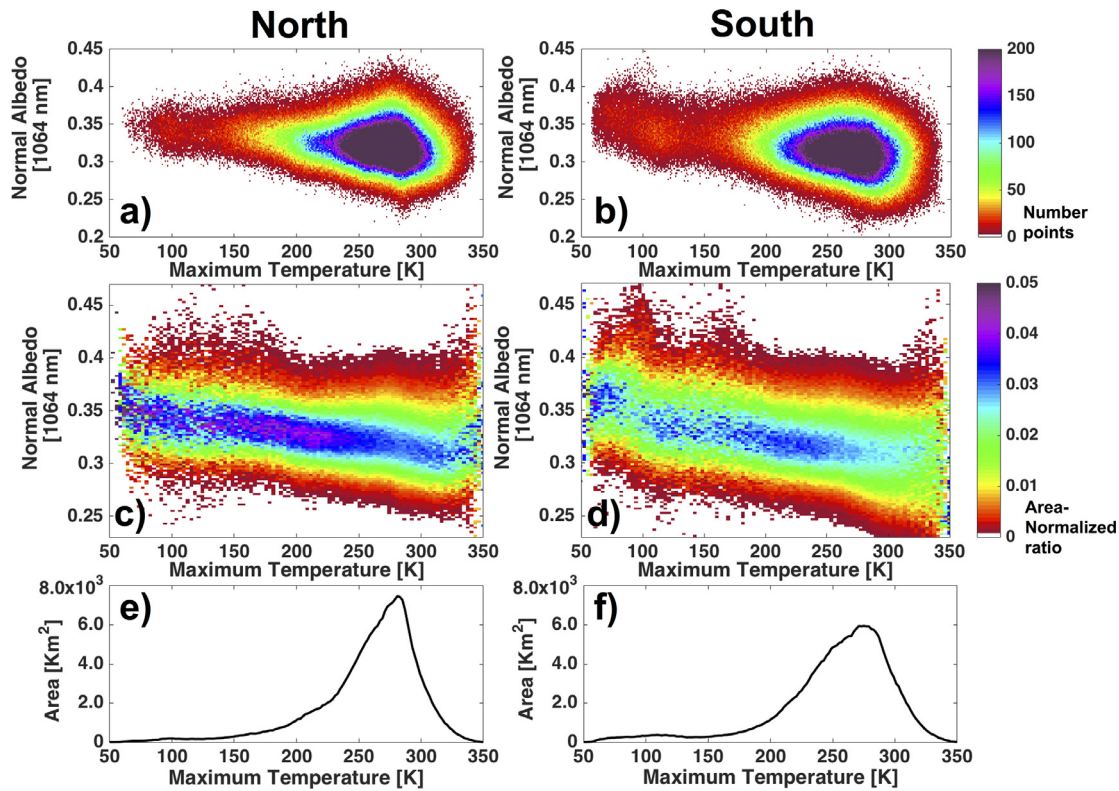
Fig. 1. Plots illustrating the relationship between Diviner maximum temperature and LOLA 1064 nm reflectance at the lunar poles (defined as regions within 20 latitude of the pole). Top: Two-dimensional histograms of 1064 nm normal albedo vs. maximum temperature for the lunar North (**a**), and South (**b**) polar regions. Normal Albedo bin width = 0.002, Maximum Temperature bin width = 1 K; Center: Two-dimensional histograms of 1064 nm normal albedo vs. maximum temperature where data within each temperature bin is normalized to the total area within that temperature bin, for the lunar North (**a**), and South (**b**) polar regions. Normal Albedo bin width = 0.002, Maximum Temperature bin width = 3 K. Histograms showing maximum temperature distribution for the North (**e**) and South (**f**) poles.

(fraction of solar disc above the horizon) and the incident flux (accounting for local slope and incidence angle) at each point (and time) along the individual LOLA profiles relevant to our study. Diviner data maximum temperatures were extracted for the latitude and longitude of each LOLA data point. The data were then spatially resampled to 500 × 500 m resolution prior to analysis to prevent biases introduced by LRO's polar orbit that features increasing sample density approaching the poles. Images of the illumination data are shown in the on-line Supplement.

3. Results

We show the relationship between 1064 nm reflectance and maximum surface temperature for the North and South polar regions (defined as within 20° of the poles) in Figs. 1 and 2. Fig. 1a and b are scatter plots or two-dimensional histograms where color denotes the total surface area that occurs within each temperature - reflectance bin. Fig. 1a and b show that the number of reflectance measurements available at different maximum temperatures varies greatly. To more clearly visualize trends, in Fig. 1c and d the two-dimensional histograms are normalized by the total area in each temperature bin. The temperature histogram used to normalized the scatter plots in 1a and 1 is shown in Fig. 1e and f.

Fig. 2 shows reflectance as a function of maximum temperature for the North (Fig. 2a) and South (Fig. 2b) polar region. The average and median values are the mean of the reflectance values within each 2 K temperature bin. The curves are plotted with 2σ (95% confidence) standard error of the mean.

Similar reflectance-temperature trends are observed in the North and South polar regions at maximum temperatures above

~150 K. First, we observe that the reflectance generally increases with decreasing maximum temperature in both polar regions. We also observe breaks in trend on the average and median reflectance curves in both polar regions. These breaks in trend occur at similar maximum temperatures in both regions: at ~200 K, ~270 K, and 300 K (Fig. 2a, b). The steep trend between ~150–200 K shallows between ~200–270 K, and steepens again between ~270–300 K. Abrupt changes in reflectance at maximum temperatures above ~350 K are caused by the statistical effect of the small number of samples in that temperature range within our study regions (Fig. 1e, f).

The reflectance-temperature behavior of the North and South polar regions differ at maximum temperatures below ~150 K. Between about 100 K and 150 K, South polar reflectance is fairly constant, while the North shows a steady rise in reflectance with decreasing temperature (Fig. 2a, b). At approximately 110 K, South polar reflectance abruptly increases, then plateaus between about 60 and 80 K (Fig. 2b). No such abrupt increase occurs in the North polar region within that temperature range (Fig. 2a). The South pole's abrupt increase in average reflectance at ~110 K is accompanied by a shift in the entire reflectance distribution (Fig. 1d, b; high reflectance outliers contribute little to the observed rise in average and median reflectance. The effect of outliers, including the effect of the bright south polar crater Shackleton, will be discussed further below. In the North, there is some evidence of a reflectance increase of similar magnitude at maximum temperatures below 80 K (Fig. 2a). However this increase coincides with a rapid decrease in available data and thus may result from sparse data within this range.
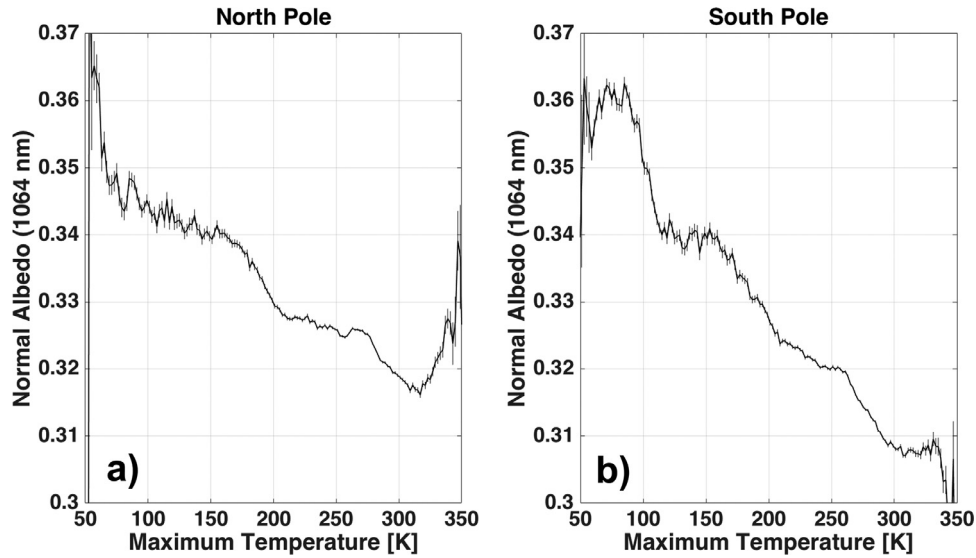
Fig. 2. Average reflectance plotted as functions of maximum temperature for the **(a)** North and **(b)** South poles. Maximum temperature bin width = 1 K. Average reflectance curves are plotted with 2σ standard error of the mean.
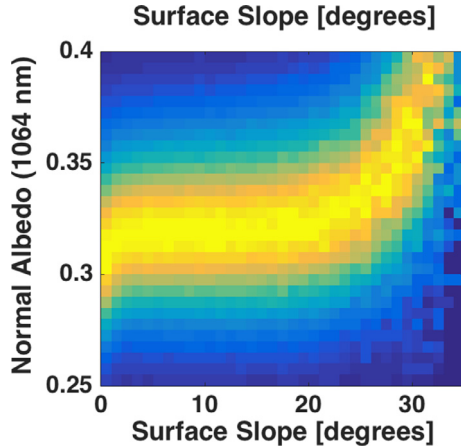

Fig. 3. Two-dimensional histogram that displays mode-normalized LOLA reflectance distribution as a function of surface slope for the North and South pole. Reflectance bin width = 0.005 and slope bin width = 1° . The strong influence of surface slope is a potential source of temperature-independent bias on the reflectance-temperature relationships observed in the polar regions.

3.1. Influence of topographic slope

Slopes steeper than ~20° promote mass wasting that exposes fresh, bright materials which have undergone less space weathering than shallow slopes which do not promote downslope movement (Lucey et al., 2014). In the polar regions, we observe that slope and reflectance data show strong positive correlation at slopes greater than 20° (Fig. 3). On slopes greater than 20° contributions to reflectance by condensed surface volatiles may be obscured by the dominant effect of mass wasting. To minimize the possibility that the reflectance-temperature trends we observe in the polar regions are caused by mass wasting, we separately investigate the temperature-reflectance behavior of steep and shallow slopes. We define shallow slopes to be less than 10° to be well separated from the influence of mass wasting, and steep slopes to be any that exceed 20°.

The temperature-reflectance behavior of polar terrain confined to low slopes and polar terrain unconstrained by slope, is similar in both the North and South at maximum temperatures below ~150 K (Figs. 2 and 4) This is expected because ~70% of our polar dataset samples terrain with slopes of less than 10°. South polar surfaces with low slopes display an abrupt increase in average reflectance below ~110 K (Fig. 4b), similar in magnitude to the ~110 K reflectance peak magnitude observed in slope-unconstrained data (~0.36) (Fig. 2b). However, at maximum temperatures above ~150 K, the temperature-reflectance behavior of low-slope and slope-unconstrained data diverges. In low-slope data, the reflectance-temperature trend breaks at ~200 K and ~300 K are weaker in both the North and South; North polar trend breaks remain visible while South polar slope trend are difficult to discern. Some difference between low-slope and slope-unconstrained data at the higher temperatures is expected because in the polar regions, higher temperatures are due to steep equator-facing slopes which are excluded in the low-slope data.

The temperature-reflectance behavior of surfaces with slopes greater than 20° is notably different than that of low-slope surfaces (Fig. 4). At the South pole, the abrupt reflectance increase at ~110 K is much greater in high-slope data (Fig. 4b). A minimum at about 120 K is also apparent in our North polar high-slope data (Fig. 4a). Additionally, South polar trend breaks and reflectance plateaus observed at maximum temperatures greater than ~150 K become more prominent on surfaces with slopes greater than 20° (Fig. 4b). In contrast, the pattern of trend breaks and plateaus above ~150 K in the North polar region is greatly subdued in high-slope data (Fig. 4a).

Because of the unknowns introduced by mass wasting on steep slopes, we primarily focus our remaining analyses to areas with slopes shallower than 10°, expected to be free of the complication of the influence of mass wasting on reflectance.

3.2. Influence of location

Latitude is known to affect lunar reflectance (Hemingway et al., 2015) and we find the temperature-reflectance behavior of low-slope (<10°) polar terrain varies significantly with proximity to the pole (Fig. 5). In the South polar region, when analysis is constrained to the immediate vicinity of the pole (85°−90°), we observe a clearly defined abrupt reflectance increase at ~110 K, whose peak magnitude (~0.37) (Fig. 5b) is similar to the ~110 K peak magnitude observed in latitude-unconstrained data (~0.36) (Fig. 4b). Near the South pole on surfaces with maximum tempera-
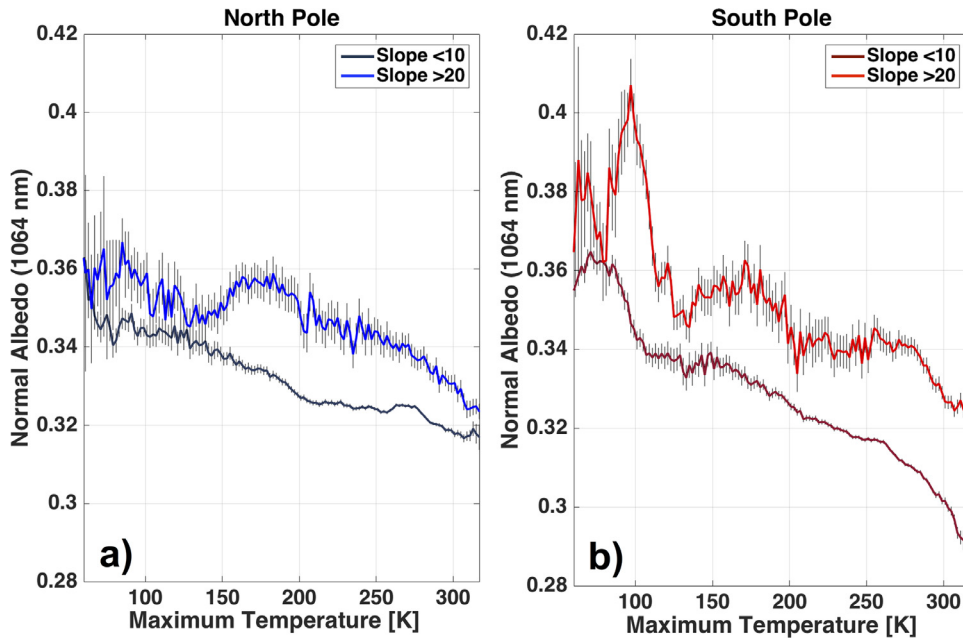
Fig. 4. Average 1064 nm reflectance as a function of maximum temperature for low slope (slope < 10°) and high slope (slope > 20°) areas for the North **(a)** and South **(b)** polar regions. Maximum Temperature bin width = 2 K. Reflectance average plotted with 2σ errors (standard error of the mean).
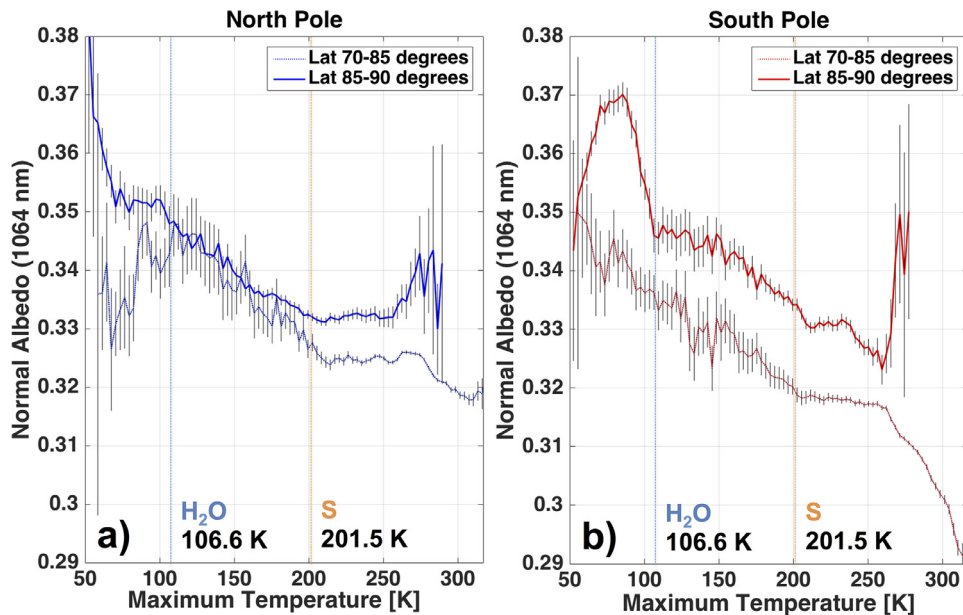

Fig. 5. Average 1064 nm reflectance as a function of maximum temperature (maximum temperature bin width = 3 K) for low slope (slope < 10°) areas free of mass wasting influence for areas within 5° of each pole, and between 5 and 20° from each pole, illustrating spatial heterogeneity in polar reflectance-temperature relationships. **a)** North polar data; **b)** South polar data. Curves plotted with 2σ standard error of the mean. Volatility thresholds for elemental sulfur and water ice are included for comparison. Thresholds were derived by Zhang and Paige (2009) a sublimation rate of 1 mm/Gyr.

tures greater than ∼110 K, the pattern of trend breaks and plateaus observed in our latitude/slope-unconstrained dataset (Fig. 2b), is replaced by a single trend break at ∼200 K followed by a steady rise in reflectance with decreasing temperature (Fig. 5b). In the North, when analysis is confined to the immediate vicinity of the pole (85°−90°), we observe a gradual but significant increase in reflectance with decreasing temperature that begins at ∼200 K, with no evidence of an abrupt reflectance increase at ∼110 K (Fig. 5a). Neither the North or South have sufficient reflectance data at maximum temperatures greater than ∼250 K to determine whether a ∼300 K trend break exists in either of the immediate polar regions (Fig. 5). In the north there is an upturn in reflectance below about

80 K that could be attributed to a frost more volatile than water ice, however the number of data points is very small and we elect not to attribute this feature to the presence of a volatile.

In the South polar region, when analysis is constrained to high latitudes away from the immediate pole (70°−85°), the abrupt ∼110 K reflectance increase observed in the immediate polar region is not observed. Instead, there is a steady increase in reflectance with decreasing temperature which starts at about 200 K (Fig. 5b). This reflectance-temperature pattern is mirrored in North high-latitude (70°−85°) data up to ∼110 K; however between about 50 and 110 K reflectance decreases instead of continuing to steadily increase (Fig. 5a). Neither the North nor South show evidence of a
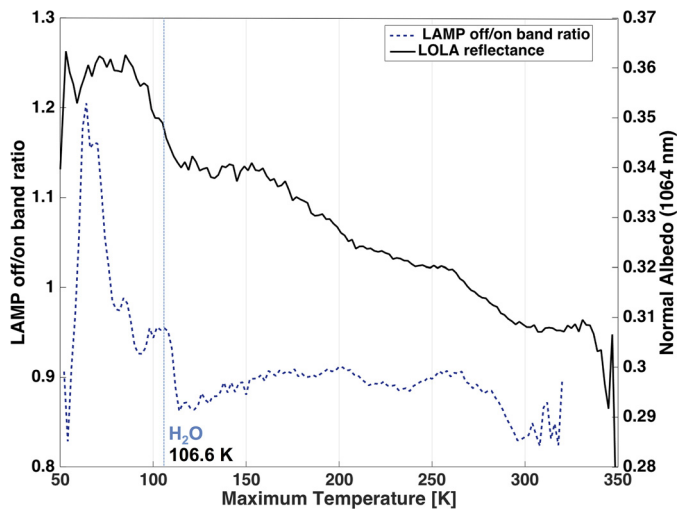
Fig. 6. Plot comparing LAMP water band ratio value (positively correlated with increasing water abundance) as a function of maximum Diviner temperature (Hayne et al., 2015), with average South polar LOLA reflectance as a function maximum Diviner temperature derived in this study. Maximum temperature bin width = 2 K. LOLA reflectance data shown include all data within 20° of the South Pole. The volatility threshold for water ice, derived by Zhang & Paige (2009) for 1 mm/Gyr is included for comparison.

trend break at ~300 K at high latitudes away from the immediate pole (70°−85°) (Fig. 5).

In summary, within 5° of the South Pole, the reflectance of surfaces rapidly increases below maximum temperatures of 110 K. This sudden increase in reflectance with decreasing temperature near 110 K is not observed at lower polar latitudes in the South Polar region and is not observed at any latitude in the North Polar region. At maximum temperatures greater than ~110 K, immediate-polar (85°−90° latitude) and high-latitude (70°−85° latitude) regions show similar patterns of temperature reflectance behavior at both poles: a sudden change in slope at ~200 K followed by steadily increasing reflectance with decreasing maximum temperature (Fig. 5).

4. Discussion

4.1. Evidence for surface water frost

The immediate South polar region (−85°−90°), exhibits reflectance-temperature behavior consistent with the presence of surface water ice, as reflectance rapidly increases below maximum temperatures of ~110 K (Fig. 5). This behavior mirrors observations made by Hayne et al. (2015) who showed that the ratio of a pair of UV wavelengths within and adjacent to a water absorption feature abruptly increases at Diviner maximum temperatures less than ~110 K in the South pole (Fig. 6), indicating the presence of surface water ice.

The North polar average and median reflectances do not show a rapid increase in reflectance below maximum temperatures of 110 K but instead show a steady increase in reflectance with decreasing temperature below about 200 K. Therefore the presence of surface frost in the North polar region is not indicated by LOLA measurements. Comparison between LOLA reflectance and LAMP water ice abundance for the North pole is not possible because north pole water ice ratio data is not currently available from LAMP (Gladstone et al., 2010, 2012).

Some prior studies reported very precise temperature values for critical maximum temperature at which surface ice is stable over geologically significant timescales derived from specifying a timescale, an ice deposit thickness and published data for

water ice vapor pressure as a function of temperature., For example Zhang and Paige (2009) reported a threshold of 106.6 K, and Schorghofer and Taylor (2007) reported a threshold of 101.3 K. The precision of these previous estimates imply that temperature-dependent reflectance transitions associated with the presence of water ice should be sharp. While the change in reflectance we observe at ~110 K is rapid compared to the general polar trend of increasing reflectance with decreasing temperature, it does occur over a somewhat wide range of temperatures (Figs. 2b, 4b and 5b). However, this broad temperature range does not preclude surface water ice as the cause of the ~110 K reflectance increase. Indeed, lunar surface characteristics as well as measurement issues can smooth the observed reflectance transitions caused by volatiles.

First, both LOLA and Diviner sample a range of temperatures within their respective footprints; these sub-pixel temperature variations are caused by a combination of low sun angle and rough topography at all scales in the polar regions which produces 'micro-cold traps' (Hayne and Aharonson, 2015). If a volatile is present in these 'micro cold-traps' below the scale of a pixel, they will increase the reflectance even if the average temperature measured by Diviner is above the nominal volatile stability threshold. Reflectance could then steadily increase with decreasing maximum temperature at the pixel scale until all the terrain within a pixel is below the stability threshold. Thus, owing to the heterogeneous nature of the lunar surface with respect to temperature below the scale of the LOLA and Diviner measurements, a very sharp transition is not expected.

Furthermore, the size and geometric difference between LOLA's and Diviner's footprints can also 'smear' temperature-dependent reflectance trends. Each Diviner measurement comprises a roughly square (~250 × 250 m) pixel, while each LOLA measurement comprises a narrow strip (~5 × 3000 m) caused by averaging 50 individual laser spots (each of which is only a few meters across) along track (Smith et al., 2010; Lemelin et al., 2016). This difference in sampling resolution means that each LOLA measurement overlaps with its corresponding Diviner maximum temperature measurement on the lunar surface, but does not cover exclusively the same area. This difference precludes the production of a sharp boundary in temperature and reflectance using our analytical methods and data, even if in reality one was present on the lunar surface.

4.1.1. Influence of Shackleton crater

Reflectance can be affected by bright geological features like fresh craters, crater rays, and impact ejecta. This raises concerns that South-polar reflectance anomalies could result from the coincidental location of anomalously reflective geology, particularly Shackleton crater, at the South pole (Zuber et al., 2012; Lucey et al., 2014).

We find that the high reflectance of the bright 20 km crater Shackleton is not responsible for the shift in reflectance mode and average we attribute to water frost. Shackleton's brightness is likely largely due to its steep walls promoting mass wasting and reflectance increase due to exposure of fresh material (Zuber et al., 2012; Lucey et al., 2014). Shackleton is situated within the South polar region where the proposed water frost signature is present and does exhibit low temperatures and so does contribute to the average reflectance. Data derived from a ~25 × 25 km box centered around Shackleton (Fig. 7b) is clearly visible as a high reflectance anomaly in the reflectance vs. maximum temperature scatter plot (Fig. 7a). However, its area is not large enough to significantly affect the reflectance average and excluding Shackleton causes only a minor shift in the position of the transition temperature threshold. (Fig. 7c). Furthermore, the steep slopes of Shackleton exclude it from the low-slope analysis (e.g. Fig. 4b). (Points in Fig. 7a. occurring at maximum temperatures near 250 K lie within the box shown in Fig. 7b, but outside the rim of Shackleton.)
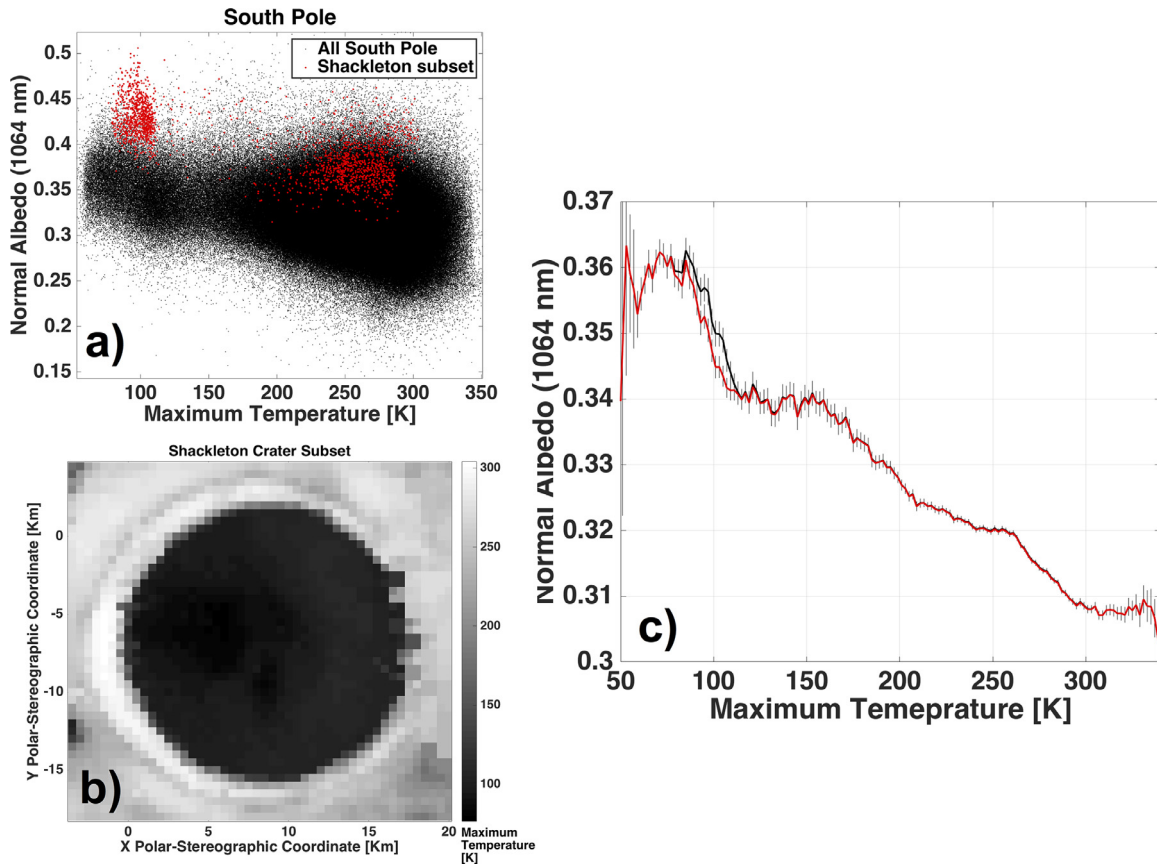
Fig. 7. a) Scatter plot of South polar reflectance vs. maximum temperature, with points in red derived from a small subset chosen to isolate South-polar Shackleton crater. Region included as red points are shown in (**b**). **c)** Curves comparing average 1064 nm reflectance as a function of maximum temperature for the south polar dataset within 20° of the pole (black), and the same data with the ~25 × 25 km Shackleton subset shown in (**b**) removed (red). Maximum temperature bin width = 2 K. Curves are plotted with 2σ standard error of the mean. Exclusion of Shackleton shifts, but does not eliminate, the sharp uptick in reflectance below 110 K. (For interpretation of the references to color in this figure legend, the reader is referred to the web version of this article.)

4.1.2. Reflectance-temperature behavior of permanently shadowed regions

The temperature of permanently shadowed regions offers an additional test of the frost hypothesis. Here permanent shadow is defined as those locations that received no solar illumination over the epoch studied by Mazarico et al. (2011). These unique environments have been shown to be brighter at 1064 nm than polar terrain that receive some illumination (Lucey et al., 2014) with frost being one of several hypotheses offered. By incorporating data from Diviner, we can directly address the effect of temperature. While PSRs do not receive direct illumination and so achieve very low temperatures, our data indicate that infrared emission from nearby illuminated walls raise some PSR temperatures above the water ice preservation temperature.

South-polar PSRs with maximum temperatures capable of maintaining stable surface water frost (less than ~110 K) show typically substantially higher reflectance than areas with maximum temperatures incapable of sustaining stable surface water frost (> 125 K), despite receiving the same negligible incident solar flux (Fig. 8d, cyan histogram (ice unstable) v. blue histogram (ice stable)). Furthermore, the average reflectance of PSRs with maximum temperatures > 125 K is similar to the average reflectance of non-PSR regions reported by Lucey et al. 2014. This shift in distributions persists at low slopes.

In North PSR regions with no slope constraints, PSR surfaces with maximum temperatures of less than 110 K are slightly brighter than warm surfaces greater than 125 K incapable of sustaining surface water frost (Fig. 8c). Low slope surfaces in the

North Pole shows at best a slight difference between the reflectance distribution and average of warm and cold surfaces (Fig. 8e).

4.2. Ice reflectance model

The distributions of reflectance within the PSRs above and below the critical ice temperature contain information on how ice may be distributed at the lower temperatures. We constructed a simple statistical model assuming the high temperature PSR reflectance distribution is representative of an ice free surface . To that population of pixels we randomly added reflective ice in various ways to attempt reproduce the low temperature distribution from the ice-free distribution. The variables in the model include the reflectance of the frost endmember, the fraction of pixels that contain ice, and the fraction of subpixel ice present in each pixel that contains ice. We applied this model to the set of pixels within South Pole PSR with maximum temperatures above 125 K to represent the frost free distribution. Fig. 9 shows the effect of adjusting several of the parameters.

We adjusted the parameters to best reproduce the shape of the distribution of the South Pole PSR with maximum temperatures below 110 K. Fig. 10 shows the distributions of reflectance values for PSRs with maximum temperatures above 125 K that cannot preserve surface ice and less than 110 K which can preserve surface ice against sublimation. The reflectance distributions of these two surfaces are distinctly shifted in average reflectance. The model that best fit the reflectance distribution of cold PSRs
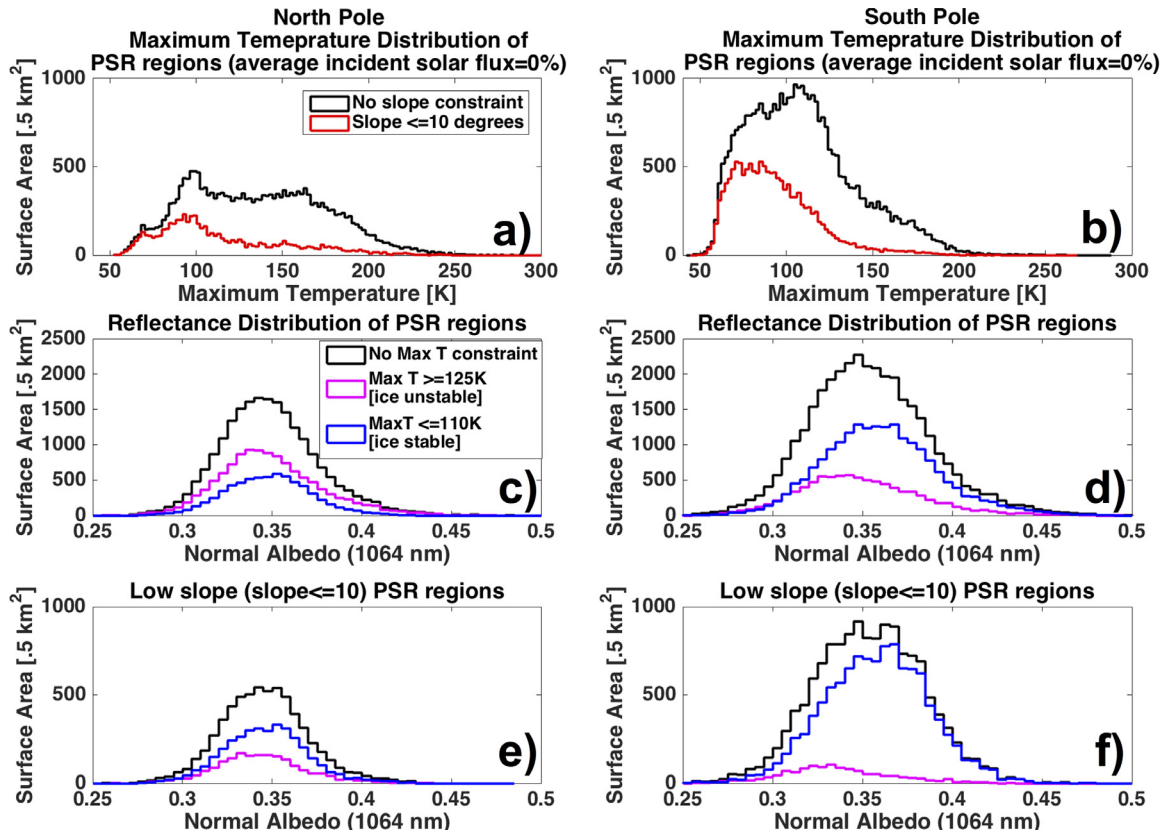
Fig. 8. a,b) Maximum temperature distribution of all PSR regions (defined as having average incident solar flux of 0%), compared to the maximum temperature distribution of low slope (slope < 10°) PSR regions, for the North (**a**) and South (**b**) poles (maximum temperature bin width = 2 K). Many portions of these PSRs exhibit maximum temperatures far above the stability threshold for water ice. **c,d)** LOLA normal albedo distribution of low temperature PSR regions capable of sustaining surface water frost (maximum temperature < 110 K, blue), compared to reflectance distribution of high temperature PSR regions incapable of sustaining surface frost (maximum temperature > 125 K magenta) at the North (**c**) and South (**d**) poles (reflectance bin width = 0.005). Reflectance distribution of PSR regions with no temperature constraints included for comparison purposes (black) (reflectance bin width = 0.005]) **e,f)** same as **c, d** but constrained to low slopes (<10°) to minimize mass wasting influence. (For interpretation of the references to color in this figure legend, the reader is referred to the web version of this article.)

is 'ice-brightened' material heterogeneously distributed (some ice-free pixels), with ice occurring at the subpixel scale (Fig. 10a). The values used were a sub-pixel ice coverage of 7%, ice reflectance of 0.8, and 75% ice bearing pixels (Fig. 10a). These agree with findings of Hayne et al. (2015) which suggest that up to 10% of the surface they observe may host surface ice on a 250 m (sub-pixel) scale, and that the distribution of this ice within low-temperature areas is highly heterogeneous. Fig. 10b shows models with predicted reflectance distribution of homogeneously distributed sub-pixel ice, and heterogeneously distributed supra-pixel (ice preserved on a scale similar to that of the LOLA pixel or larger). Models that contained ice within every pixel could not match both the symmetry and mode of the reflectance histogram of the low temperature PSR surfaces. Models that included some pixels with 100% ice cover produced high reflectance modes that are not observed.

4.3. Evidence for other volatiles

At temperatures above ~110 K, the North and South poles show a pattern of 'trend breaks', which initiate at ~200 K and ~300 K, where reflectance average and median increase rapidly with decreasing maximum temperature (Fig. 2a and b). When confined to shallow slopes, the ~200 K temperature transition remains prominent in both high-latitude (70°−85°) and immediate-polar (85°−90°) regions, and occurs at both poles, suggesting that it may arise from a widespread reflectance-altering process acting on both polar regions and not random geological variation (Fig. 5a, b). Since

its behavior is reminiscent of the rapid reflectance increase near ~110 K that we attribute to surface water frost, it is possible that this ~200 K reflectance transition is caused by the deposition of additional volatile species.

As previously discussed, the temperature ranges over which reflectance transitions caused by volatile deposition occur are likely blurred by micro-cold trapping and differences between the Diviner and LOLA footprint. The broad temperature range over which each of our observed ~200 K reflectance transitions occurs allows a wide range of plausible volatile stability thresholds, and includes many potential volatile candidates. Volatile species with stability thresholds between ~150K and 210 K include various species of aromatic hydrocarbons, linear amides, and carboxylic acids, in addition to elemental sulfur (Zhang and Paige, 2009). Sulfuretted species detected in the Cabeus PSR by the LCROSS impact experiment could conceivably be produced by reactions including elemental sulfur in the impact plume (Colaprete et al., 2010). Additionally, Zhang and Paige (2009) suggested that the presence of elemental sulfur in addition to water may indicate contribution from lunar volcanic processes.

Although it is possible that the ~300 K reflectance transition we observe in our slope-unconstrained dataset could be influenced by mass wasting, volatile species with stability thresholds between ~260K and 310 K do exist. Such volatile candidates are less common, but include some more complex polycyclic aromatic hydrocarbons, including coronene (De Vries et al., 1991; Chickos et al., 2002). Simple organics have been suggested as responsible for dark polar deposits on Mercury (Paige et al., 2013), and these species
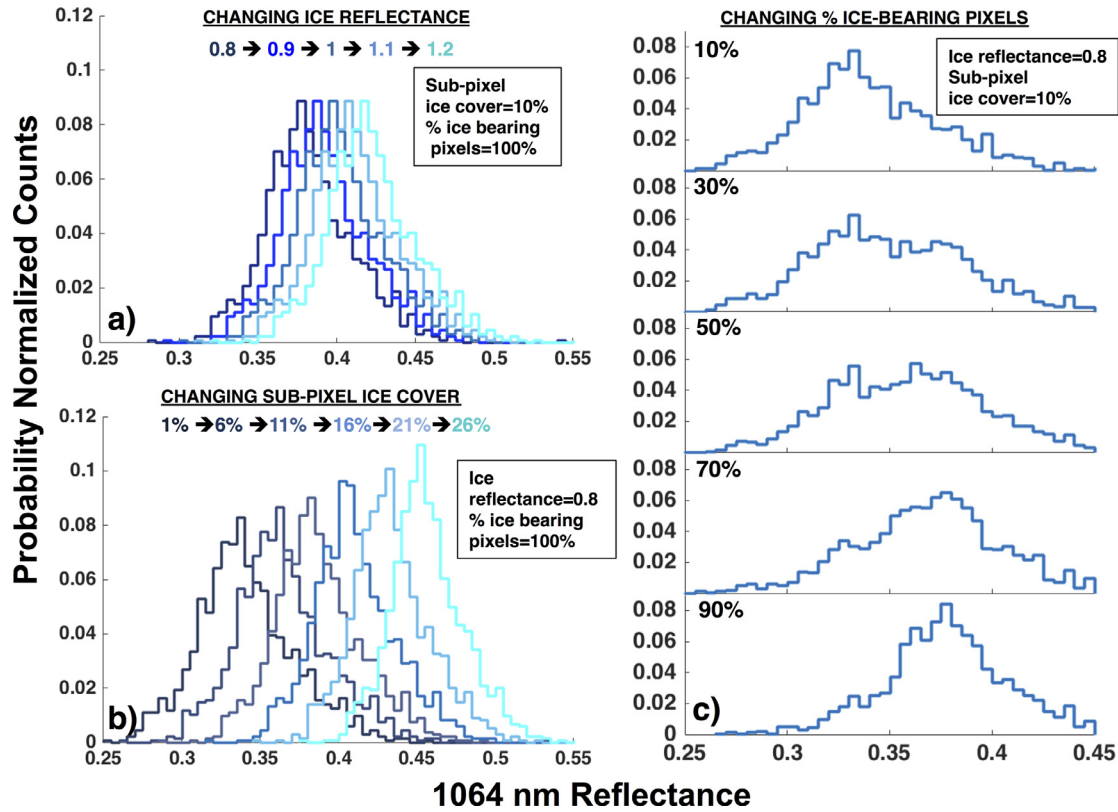
Fig. 9. Results showing the effect of varying our three ice model input parameters: 'ice reflectance' **(a)**, 'sub-pixel ice cover' **(b)**, and 'percent ice bearing pixels' (ice-heterogeneity) **(c)**. This model applies ice-brightened material to an ice free distribution via linear mixing. The ice-free starting distribution was we chose the reflectance distribution of low slope (slope < 10°) South-polar PSRs (average incident flux = 0%), with maximum temperatures high enough (>125 K) to preclude the preservation of surface ice. Reflectance bin width of all histograms equals 0.005.
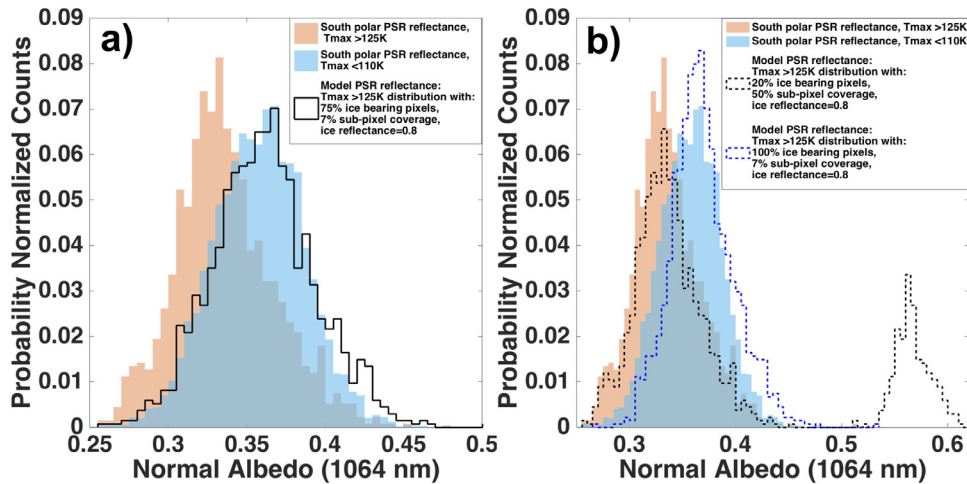

Fig. 10. Results of some combinations of ice-modeling parameters consistent with plausible modes of ice preservation, compared to the real reflectance distributions of low slope (slope < 10°) South-polar PSRs (average incident flux = 0%), with maximum temperatures low enough (<110 K) to preserve surface ice (filled blue), and high enough (>125 K) to preclude the preservation of surface ice (filled orange). Reflectance bin width = 0.005. **a)** results of adding sub-pixel scale, heterogeneously distributed icy material to the reflectance distribution of ice-free south polar PSRs (black solid line). **b)** results of adding sub-pixel scale, homogeneously distributed icy material (black dashed line), and supra-pixel scale heterogeneously distributed icy material (blue dashed line) to the reflectance distribution of ice-free south polar PSRs. (For interpretation of the references to color in this figure legend, the reader is referred to the web version of this article.)

may be emplaced at the lunar poles via cometary ices, galactic cosmic ray exposure (Crites et al., 2013), or micrometeorites (Bruk-Syal et al., 2015).

4.4. General trends of temperature and reflectance

The temperature-reflectance trend breaks discussed above are superimposed upon a broad negative correlation between maxi-mum temperature and reflectance (Figs. 1, and 2). This trend is apparent at both poles and occurs independently of mass wast-ing, as it is apparent in both low-slope (<10°) and high-slope (>20°) areas (Fig. 4a, b). Recently Hemingway et al. (2015) showed that the reflectance of the lunar maria is correlated with lati-tude, and suggested that this effect was caused by weakening of space weathering as solar wind, proxied by incident solar flux, de-

creases proportional to latitude. Since maximum temperature and average incident solar flux are proportional, the general reflectance-temperature correlation we observe are consistent with this solar-wind dependent space weathering.

There is also evidence that the space weathering process itself is affected by temperature. Space weathering simulated in the laboratory using pulsed laser irradiation by Corley et al. (2016) found that particulate samples irradiated at ∼100 K darkened less than samples irradiated at 300 K for the same amount of exposure to laser irradiation. This dependence of space weathering efficiency on temperature may be influencing the general temperature-reflectance trends we observe.

4.5. Distribution of candidate ice locations

This study has argued that the onset of a sudden increase in reflectance at temperatures below 110 K is an indication of the potential presence of surface water ice; this argument mirrors that of Paige et al. (2013), who related a sudden increase in reflectance at 110 K with the presence of water ice on Mercury. Based on this reasoning, we developed an algorithm to partially map the distribution of potential ice-rich locations at the lunar poles.

We note that making definitive statements about whether particular locations host ice is difficult because of the strongly overlapping reflectance distributions of cold (<110 K) ice-brightened and ice-free areas, which are likely distributed heterogeneously within PSRs. However, we are able to identify areas that are so reflective that they are quite unlikely to be members of the background variation in reflectance due to ordinary lunar geologic processes. We identify those areas by first computing the statistics of the reflectance distribution of polar areas with maximum temperatures too warm to support the presence of surface ice. We then compare the reflectance distribution of polar areas cold enough to support surface ice with the statistics of the 'ice-free' reflectance distribution defined above.

The general trend of increasing reflectance with decreasing temperature (Fig. 1) complicates use of the simple metric of anomalous reflectance as an indicator of the presence of ice. Under the assumption that this general trend is unrelated to processes involving surface water frost in areas with maximum temperatures greater than 125 K, we fit the reflectance-temperature data of ice free (>125 K) areas at each pole with a linear trend. We then removed this linear trend from the entire reflectance distribution of each pole, resulting in temperature-corrected normal albedo free of temperature correlated brightening effects unrelated to the presence of ice. This removes the general bias toward higher reflectance present at both poles to the degree that the trend is linear.

For each pole, we then selected all areas with maximum temperatures between 125 and 175 K to represent the statistics of the ice-free polar background and its variations in reflectance imposed by geologic processes. We calculated the mean and standard deviation of the temperature-corrected normal albedo for these background areas, then compared the reflectance distribution of polar areas cold enough to support surface ice with the statistics of the 'ice-free' reflectance distribution defined above. Areas with maximum temperatures below 110 K that were 2-sigma more reflective than the mean reflectance of the ice-free distribution at each pole, and with surface slopes less than 10°, are identified as potentially hosting surface water frost; these anomalously bright pixels are mapped for the North and South in Fig. 11.

Fig. 11 shows that in the South Pole the distribution of anomalously reflective locations is consistent with our observations regarding the shape of the reflectance temperature curve and latitude as described in Section 3.2. The anomalous reflectance sig-
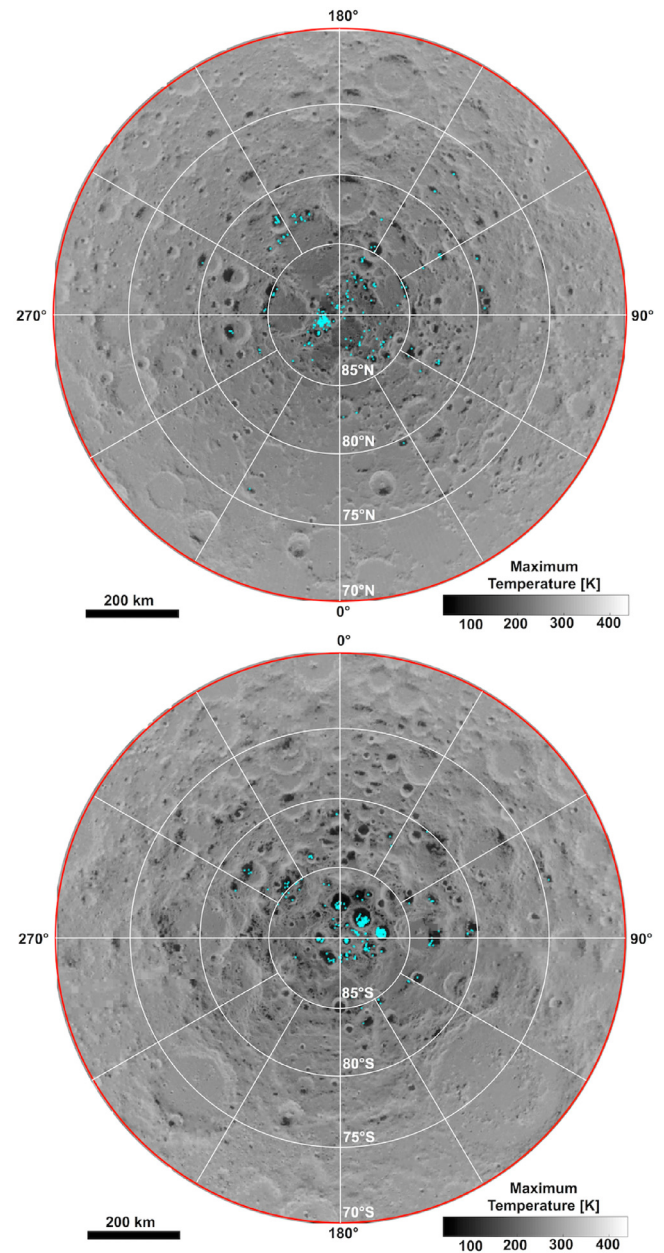

Fig. 11. Detection maps of anomalously bright pixels in the north (top) and south (bottom). Cyan pixels are show the locations of surfaces that are brighter than 2-sigma than the mean of the 125–175 K population of pixels that have maximum temperatures between 125 and 175 K, and have maximum temperatures less than 110 K and slopes less than 10°. At both poles there are concentrations of pixels that indicate a common brightening process. Being brighter than 2-sigma, these clusters are unlikely to be part of the background ice-free population.

nal appears to be limited to surfaces within 5° of the South Pole, and that the great majority of anomalously reflective pixels occur within the craters Shoemaker, Haworth, Faustini, Shackleton, de Gerlache, Sverdrup and Slater, as well as small unnamed craters within the perimeter formed by these larger craters.

At the North Pole anomalous pixels are also present, a result that is not unexpected because some pixels within the ice-free background's reflectance distribution will necessarily deviate more than 2 sigma from the background reflectance mean. However, these anomalous pixels are not randomly distributed, but are largely concentrated in a small irregular region of scattered permanent shadow within a triangle formed by the craters Aepinus,

Hinshelwood and Hermite A, suggesting a geologic control on their distribution.

We emphasize that these maps of anomalous pixels are not comprehensive maps of candidates for ice rich surfaces. These are the locations where the corrected reflectance is so high that they are very unlikely to be due to ordinary geologic processes, as defined by the statistics of nearby areas that experience higher maximum temperatures. However, ice may be present throughout the area near the South Pole exhibiting maximum temperatures less than 110 K. The cluster of flagged pixels near the North Pole constitute detections by the definitions given in this section. However, the general temperature reflectance behavior of the North pole appears not to be affected by the presence of ice or other temperature dependent reflectance enhancing processes that begin to operate below 110 K.

5. Conclusions

We find that 1064 nm LOLA reflectance near the lunar South pole abruptly increases at Diviner maximum surface temperatures below ∼110 K, behavior consistent with the presence of persistent surface water ice deposits. This abrupt change in reflectance with temperature is observed in some, though not all, of the lunar polar shadowed regions. This is consistent with the conclusions of Hayne et al. (2015) arrived at using UV frost ratio data from LAMP compared to Diviner temperatures. The ∼110 K maximum temperature threshold where we observe this increase in reflectance is consistent with several previously calculated estimates of water-ice's stability threshold, all on the order of ∼100 K (Schorghofer and Taylor, 2007; Zhang and Paige, 2009; Siegler et al., 2016; Paige et al., 2013; Hayne et al., 2015). The reflectance behavior of the lunar South pole mirrors that of the north polar region of Mercury, which shows rapidly increasing 1064 nm reflectance at modeled maximum temperatures below ∼100 K, attributed to the presence of surface water frost in Mercury's cold traps (Neumann et al., 2013; Paige et al., 2013). The lunar north pole does not exhibit a regional sudden increase in reflectance below ∼100 K.

We do find local concentrations of anomalously bright pixels at both poles. We highlighted those pixels that are more reflective than two sigma over the mean reflectance of surfaces with maximum temperatures >125 K, corrected for the general temperature-reflectance trend. In the South, we interpret these as being the brightest members of a general population of surfaces that appear to be brightened by ice based on the presence of the excursion in reflectance below 110 K. The north does not show the sudden increase at 110 K in its temperature-reflectance curve, but the cluster of pixels identified are clearly anomalous and may represent a more limited exposure of surface frost than at the South Pole.

We rule out mass wasting influence as the cause of South polar brightening below ∼110 K, by controlling our analysis for slope. Additionally, if slope-dependent mass wasting processes can create sudden chances in reflectance distribution, this should also be occurring in our studied North polar region where an increase in reflectance below ∼100 K is not observed.

Previous results showed that PSRs are in general brighter than surrounding terrain that is sometimes illuminated (Lucey et al., 2014). However, we find that surface brightening observed in South polar PSRs is primarily a function of temperature, and not illumination, by showing that the average reflectance and reflectance mode of South polar PSRs with maximum temperatures below 110 K (capable of sustaining surface water ice), are significantly brighter than those of PSRs that maintain maximum temperatures above 125 K (incapable of sustaining surface water ice), and that the warmer PSRs have reflectance similar to terrain that is sometimes illuminated.

A model that accounts for the mean and shape of the distribution of reflectances in the PSRs indicates a sub-pixel ice coverage of 7%, ice reflectance of 0.8, and 75% ice bearing pixels, consistent with the previous results of Hayne et al. (2015).

We observe abrupt reflectance increases at maximum temperatures near ∼200 K and ∼300 K that may indicate the presence of other volatiles, such as sulfur or organics. The same pattern is observed at both poles, an indicator of a general process.

There is a general trend of increasing reflectance with decreasing maximum temperature; this trend is consistent with a space weathering trend as solar wind sputtering, average solar flux and maximum temperature are correlated. Recent experiments show that the space weathering process itself may be inhibited by low temperatures, and this also may contribute to the observed effects.

Finally, unlike the north pole of Mercury, where all surfaces below about 100 K exhibit reflectance anomalies, on the Moon this increase in reflectance with decreasing temperature is confined to the region immediately around the South pole. A similar characteristic is observed in the UV water ice ratio in the South polar region by Hayne et al. (2015). At lower southern latitudes and at the North pole, we do not observe a sudden increase in reflectance below maximum temperatures of 100 K, though a cluster of anomalously reflective pixels are present near the North Pole The generally poor correlation of volatile signatures and temperature at the lunar poles–despite the localized detections reported here and by Hayne et al. (2015)–stands in stark contrast with Mercury where temperature accurately predicts ice distribution. This Moon-Mercury difference remains an outstanding question in lunar science (Siegler et al. 2016).

Supplementary materials

Supplementary material associated with this article can be found, in the online version, at doi:10.1016/j.icarus.2017.03.023.

References

Andreas, E.L., 2007. New estimates for the sublimation rate for ice on the Moon. Icarus 186 (January(1)), 24–30.

Chabot, N.L., et al., 2014. Images of surface volatiles in Mercury's polar craters acquired by the MESSENGER spacecraft. Geology 42 (12), 1051–1054. doi:10.1130/G35916.1.

Chickos, J.S., Webb, P., Nichols, G., Kiyobayashi, T., Cheng, P.-C., Scott, L., 2002. The enthalpy of vaporization and sublimation of corannulene, coronene, and perylene at T=298.15 K. J. Chem. Thermodyn. 34 (8), 1195–1206. doi:10.1006/jcht.2002.0977.

Colaprete, A., et al., 2010. Detection of water in the LCROSS Ejecta Plume. Science 330 (6003), 463–468. doi:10.1126/science.1186986.

Corley, L.M., Gillis-Davis, J.J., Lucey, P.G., Trang, D., 2016. Space weathering at the Lunar poles: the effect of temperature on reflectance of materials weathered by laser irradiation. Lunar Planet. Sci. Conf., XLVII abstract no. 2692.

Crites, S.T., Lucey, P.G., Lawrence, D.J., 2013. Proton flux and radiation dose from galactic cosmic rays in the lunar regolith and implications for organic synthesis at the poles of the Moon and Mercury. Icarus 226 (2), 1192–1200. doi:10.1016/j.icarus.2013.08.003.

Gladstone, G.R., et al., 2010. LAMP: the lyman alpha mapping project on NASA's Lunar reconnaissance orbiter mission. Space Sci. Rev. 150 (1-4), 161–181. doi:10.1007/s11214-009-9578-6.

Gladstone, G.R., et al., 2012. Far-ultraviolet reflectance properties of the Moon's permanently shadowed regions. J. Geophys. Res. Planets 117 (E12), E00H04. doi:10.1029/2011JE003913.

Goddard, R.H., 1920. In: Goddardand, E.C., Pendray, G.E. (Eds.). In: Papers of Robert H. Goddard, Volume 1. McGraw-HiH, 1970, New York, pp. 413–430.

Hayne, P.O., Aharonson, O., 2015. Thermal stability of ice on Ceres with rough topography. J. Geophys. Res. Planets 120 (9), 1567–1584. doi:10.1002/2015JE004887.

Hayne, P.O., Hendrix, A., Sefton-Nash, E., Siegler, M.A., Lucey, P.G., Retherford, K.D., Williams, J.-P., Greenhagen, B.T., Paige, D.A., 2015. Evidence for exposed water ice in the Moon's south polar regions from Lunar Reconnaissance Orbiter ultraviolet albedo and temperature measurements. Icarus 255, 58–69. doi:10.1016/j.icarus.2015.03.032.

Hemingway, D.J., Garrick-Bethell, I., Kreslavsky, M.A., 2015. Latitudinal variation in spectral properties of the lunar maria and implications for space weathering. Icarus 261, 66–79. doi:10.1016/j.icarus.2015.08.004.

Lawrence, D.J., Hurley, D.M., Feldman, W.C., Elphic, R.C., Maurice, S., Miller, R.S., Prettyman, T.H., 2011. Sensitivity of orbital neutron measurements to the thickness and abundance of surficial lunar water. J. Geophys. Res. 116, E01002. doi:10.1029/2010JE003678.

Lemelin, M., Lucey, P.G., Neumann, G.A., Mazarico, E.M., Barker, M.K., Kakazu, A., Trang, D., Smith, D.E., Zuber, M.T., 2016. Improved calibration of reflectance data from the LRO Lunar Orbiter Laser Altimeter (LOLA) and implications for space weathering. Icarus 273, 315–328. doi:10.1016/j.icarus.2016.02.006.

Lucey, P.G., et al., 2014. The global albedo of the Moon at 1064 nm from LOLA. J. Geophys. Res. Planets 119 (7), 1665–1679. doi:10.1002/2013JE004592.

Mazarico, E., Neumann, G.A., Smith, D.E., Zuber, M.T., Torrence, M.H., 2011. Illumination conditions of the lunar polar regions using LOLA topography. Icarus 211 (2), 1066–1081. doi:10.1016/j.icarus.2010.10.030.

Mitrofanov, I, Litvak, M, Sanin, A, Malakhov, A, Golovin, D, Boynton, W, Droege, G, Chin, G, Evans, L, Harshman, K, Fedosov, F, 2012 Dec 1. Testing polar spots of water-rich permafrost on the Moon: LEND observations onboard LRO. J. Geophys. Res. 117 (E12).

Neumann, G.A., Cavanaugh, J.F., Sun, X., Mazarico, E.M., Smith, D.E., Zuber, M.T., Mao, D., Paige, D.A., Solomon, S.C., Ernst, C.M., Barnouin, O.S., 2013. Bright and dark polar deposits on Mercury: Evidence for surface volatiles. Science 339 (6117), 296–300.

Paige, D.A., et al., 2010a. Diviner lunar radiometer observations of cold traps in the Moon's south polar region. Science 330 (6003), 479–482. doi:10.1126/science.1187726.

Paige, D.A., et al., 2010b. The Lunar reconnaissance orbiter diviner Lunar radiometer experiment. Space Sci. Rev. 150 (1-4), 125–160. doi:10.1007/s11214-009-9529-2.

Paige, D.A., Siegler, M.A., Harmon, J.K., Neumann, G.A., Mazarico, E.M., Smith, D.E., Zuber, M.T., Harju, E., Delitsky, M.L., Solomon, S.C., 2013. Thermal stability of volatiles in the north polar region of Mercury. Science 339 (6117), 300–303. doi:10.1126/science.1231106.

Schorghofer, N., Taylor, G.J., 2007. Subsurface migration of H_2O at Lunar cold traps. J. Geophys. Res. 112 (E2), E02010. doi:10.1029/2006JE002779.

Siegler, M.A., Miller, R.S., Keane, J.T., Laneuville, M., Paige, D.A., Matsuyama, I., Lawrence, D.J., Crotts, A., Poston, M.J., 2016. Lunar true polar wander inferred from polar hydrogen. Nature 531 (7595), 480–484.

Smith, D.E., Zuber, M.T., Jackson, G.B., Cavanaugh, J.F., Neumann, G.A., Riris, H., Sun, X., Zellar, R.S., Coltharp, C., Connelly, J., Katz, R.B., 2010. The Lunar orbiter laser altimeter investigation on the Lunar reconnaissance orbiter mission. Space Sci. Rev. 150 (1), 209–241.

Syal, M.B., Schultz, P.H., Riner, M.A., 2015. Darkening of Mercury's surface by cometary carbon. Nat. Geosci. 8 (5), 352–356. doi:10.1038/ngeo2397.

De Vries, M.S., Wendt, H.R., Hunziker, H., Peterson, E., Chang, S., 1991. Search for high molecular weight polycyclic aromatic hydrocarbons and fullerenes in carbonaceous meteorites. Abstr. Lunar Planet. Sci. Conf. 22, 315–316 (abstract).

Urey, H.C., 1952. The Planets: Their Origin and Development. Yale University Press, New Haven, CT.

Watson, K, Murray, BC, Brown, H, 1961. The behavior of volatiles on the lunar surface. J. Geophys. Res. 66 (September(9)), 3033–3045.

Wessel, P., Smith, W.H.F., 1991. Free software helps map and display data. EOS Trans. AGU 72, 441.

Zhang, J.A., Paige, D.A., 2009. Cold-trapped organic compounds at the poles of the Moon and Mercury: implications for origins. Geophys. Res. Lett. 36 (16). doi:10.1029/2009GL038614.

Zuber, M.T., et al., 2012. Constraints on the volatile distribution within Shackleton crater at the Lunar south pole. Nature 486 (7403), 378–381. doi:10.1038/nature11216.